Chemical Engineering Journal 162 (2010) 956–964

Contents lists available at ScienceDirect

Chemical Engineering Journal

journal homepage: www.elsevier.com/locate/cej

Hydrodynamic drag and rise velocity of microbubbles in papermaking process waters

Antti Haapala[a,*], Markus Honkanen[b], Henrikki Liimatainen[a], Tuomas Stoor[a], Jouko Niinimäki[a]

[a] *University of Oulu, Fibre and Particle Engineering Laboratory, P.O. Box 4300, FIN-90014, Finland*
[b] *Tampere University of Technology, Energy and Process Engineering, P.O. Box 589, FIN-33101, Finland*

ARTICLE INFO

Article history:
Received 20 March 2010
Received in revised form 28 June 2010
Accepted 1 July 2010

Keywords:
Bubble dynamics
Hydrodynamic drag
Image analysis
Multiphase flow
Separations

ABSTRACT

Diversity of dissolved, colloidal and solid materials present in papermaking process waters influences the rise of microbubbles by increasing their drag. This effect is known to reduce the gas separation efficiency but its importance thus far has not been quantified by experimental studies. In this paper the terminal velocities and drag coefficients of bubbles as a function of the bubble Reynolds number are studied experimentally in papermaking process waters with a high-speed CMOS camera and a submersed backlight illumination in a pressurised bubble column. Bubbles are tracked in time to provide time series data for every bubble that passes the focal plane of the imaging system. Image sequences are analysed with automatic image processing algorithms that measure the velocity and size of bubbles, and also the velocity of the fluid surrounding the bubbles revealing the instantaneous slip velocity of each bubble. Results show how suspension viscosity, surface tension and solids content affect the kinetics of microbubbles. Changes in microbubble formation during a pressure drop and differences of bubble size distributions in a variety of process waters and model solutions are also shown. Finally, an empirical correlation between the bubble drag coefficient and the bubble Reynolds number is generated for the investigated process waters.

1. Introduction

Bubbly gasses and their interaction with other substances in process waters and pulp suspensions may cause substantial problems in papermaking processes. Most of the problems relate to stock filtration, dewatering, sheet formation or pumping but also to process measurements, as presented by Stoor [1]. Therefore, gas removal i.e. deaeration is a highly important part of a papermaking process. Deaeration usually takes place in a pressurised tank or a special gas removal pump, while some passive methods rely solely on the bubble rise and the evacuation from suspension. Today, different solutions for gas removal are developed using mathematical models and computational fluid dynamics (CFD) tools that strive to describe the complex phenomenon of the bubble motion in a multiphase environment, and typically turbulent flow conditions. These models require experimental knowledge on the kinetics and hydrodynamics behind the free gas bubble rise in actual process suspensions. The aim of the study is to investigate the effect of process water properties on size distribution and the motion of microbubbles in white waters in order to produce consistent experimental data for the validation of multiphase CFD models.

The rise of free gas bubbles in liquids and suspensions is hindered by viscosity and solids. On the other hand, surface tension of the liquid phase affects the size distribution of formed bubbles, as noted by Okazaki [2], Reese et al. [3], Garver et al. [4], Margaritis et al. [5], Heindel [6] and Hubbe [7]. These effects are typical for filtration waters from a sheet former with low fibre content, commonly referred as *white waters*. The suspended solids are the main components contributing to the bubble drag in white waters i.e. fibre fines fractions and inorganic particles such as clay fillers [4,7]. Their composition and overall chemical state varies from one paper machine to another, while process waters slowly accumulate dissolved and colloidal materials from raw materials, process chemicals and fresh water until steady-state levels are reached. While the effect of surfactants on the drag coefficient of rising bubbles was shown in the work of Okazaki [8], so far experimental research on the bubble drag and rise velocity in papermaking white waters has not been published.

Image-based measurements have become a powerful tool to determine the gas bubble size, velocity and the velocity of suspension surrounding gas bubbles. Robust image analysis algorithms [8,9] can automatically recognise individual bubbles from image sequences of complex multiphase suspensions, where bubble images commonly overlap each other. Optical measurements are, however, limited to dilute multiphase flows, as they require undisturbed optical access to the measurement volume. Dispersed phase

---

* Corresponding author. Tel.: +358 8 5532420; fax: +358 8 5532405.
E-mail address: Antti.Haapala@oulu.fi (A. Haapala).

1385-8947/$ – see front matter © 2010 Elsevier B.V. All rights reserved.
doi:10.1016/j.cej.2010.07.001

Table 1
Properties of white waters 1–8 (denoted as WW #).

	WW1	WW2	WW3	WW4	WW5	WW6	WW7	WW8
pH (20 °C)	7.9	4	6.9	7.7	7.7	7.7	7.7	7.6
Density (40 °C) [g/L]	988	989	988	987	991	991	995	989
Conductivity (20 °C) [μS/cm]	1.50	2.00	1.00	0.90	1.00	0.90	1.10	1.40
Dry matter content [%]	0.58	0.49	0.5	0.25	0.22	0.22	0.25	0.21
Surface tension (20 °C) [mN/m]	53	51	48	59	58	53	66	61
Apparent viscosity (40 °C) [mPa s]	1.7	1.8	1.8	1.4	1.3	1.2	1.4	1.5
Mean particle size (from <90%) [μm]	7.9 (20.7)	10.0 (26.3)	6.5 (20.8)	7.3 (23.6)	7.4 (20.0)	8.3 (26.3)	10.4 (33.3)	7.1 (19.4)

particles and bubbles in these suspensions scatter the incident light and weaken the light intensity, which restricts the penetration of light through the suspension. However, intrusive experimental methods such as an underwater camera probe [10] provide a way to visualise these opaque multiphase suspensions inside large vessels. In this study, the bubbly multiphase flows are visualised near the transparent column wall with a high-speed CMOS camera and submerged back-light illumination optics. Bubbles are tracked in time to provide time series data of bubble size and velocity and the velocity of the surrounding fluid for every bubble that passes the measurement plane. These results include the bubble size distributions, rise velocities and bubble drag coefficients (C_D) for each white water as a function of the bubble Reynolds number.

2. Materials and methods

2.1. Studied suspensions

The examined white waters (denoted here as WWs) originate from 8 European paper machines that utilise a wide range of raw materials and produce a variety of paper grades: mechanical pulp to produce newsprint and magazine grades while eucalyptus, pine or similar kraft pulp to produce different fine paper grades. Thus, fines and fillers content in white waters varied accordingly for each machine. Waters 1–3 and 5 contain wood fines from thermomechanical pulp while the bulk of organic solids in waters 4 and 6–8 originate from bleached chemical kraft pulp.

To determine the composition of each white water, analyses were made according to the following standards and methods: pH (SFS 3021), conductivity (SFS-EN 27888) and dry matter content (SFS-EN 20638). Surface tension was measured with a Krüss K8600 (du Noüy's ring method) and viscosities with a Haake 501 viscometer and NV spindle at 3200 rpm. In addition, the mean particle size of white water solids was determined using a multi-wavelength particle size analyser (Beckman Coulter LS 13 320). Physico-chemical properties of tested white waters are summarised in Table 1.

In addition to process waters, measurements were made on model waters to investigate the effect of individual suspension properties on microbubble kinetics and size distribution. Carboxymethyl cellulose (CMC) and n-butanol were added into water in the absence and presence of dry refined pine kraft pulp fibres (average fibre length 1.52 mm). CMC was used to increase the viscosity, n-butanol to lower suspension surface tension and wood fibres to promote microbubble formation through nucleation and also to increase the bubble drag through bubble–solid interactions in model waters. Microbubble motion in a variety of these suspensions was measured similar to process waters. Properties of these model waters are presented in Table 2. Tap water differed from pure deionised water by having a slightly lower surface tension of 70 mN/m (Table 2). Lower surface tension indicates a presence of contaminants in water.

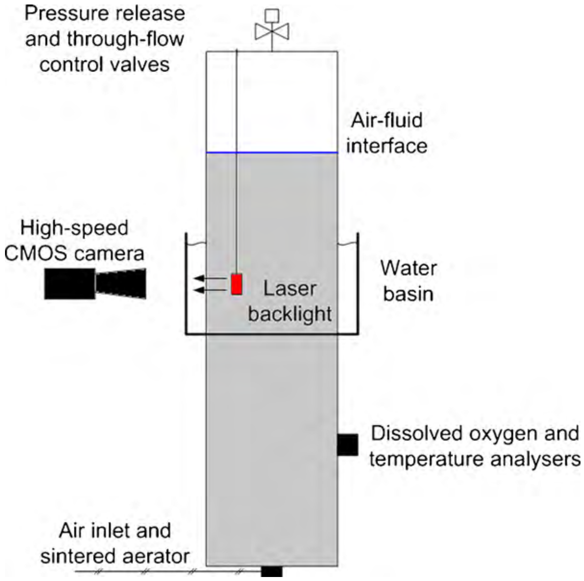

Fig. 1. Experimental setup consisting of a pressurised bubble column and camera.

2.2. Measurement setup

Experiments were carried out in a closed, pressurised bubble column. 20 litres of suspension was pressurised inside a 1200 mm long cylindrical bubble column with a diameter of 167 mm. A steady internal pressure of 300 kPa was maintained by feeding pressurised air at 25 °C through a sintered porous media at 400 kPa, allowing a continuous flow of air through the column. The amount of dissolved oxygen in the water increased until the suspension saturation level was reached. This was monitored by a dissolved oxygen analyser (Hach Orbisphere 3600).

After saturating the suspension with an air feed, a pressure drop was created by opening a solenoid valve on top of the column. Images of generated microbubbles were gathered over a period of 30 s after the first microbubble appeared in the measurement volume. Illustration of the experimental setup is presented in Fig. 1. Imaging took place through a 300 mm high midsection of trans-

Table 2
Properties of model suspensions.

	Water	CMC	CMC + fibre	n-Butanol	n-Butanol + fibre
pH (20 °C)	8.6	–	–	–	–
Dry matter content [%]	0	0	0.15	0	0.15
Surface tension (20 °C) [mN/m]	70	68	70	54	54
Apparent viscosity (20 °C) [mPa s]	1	5.6	58	1.5	2.2

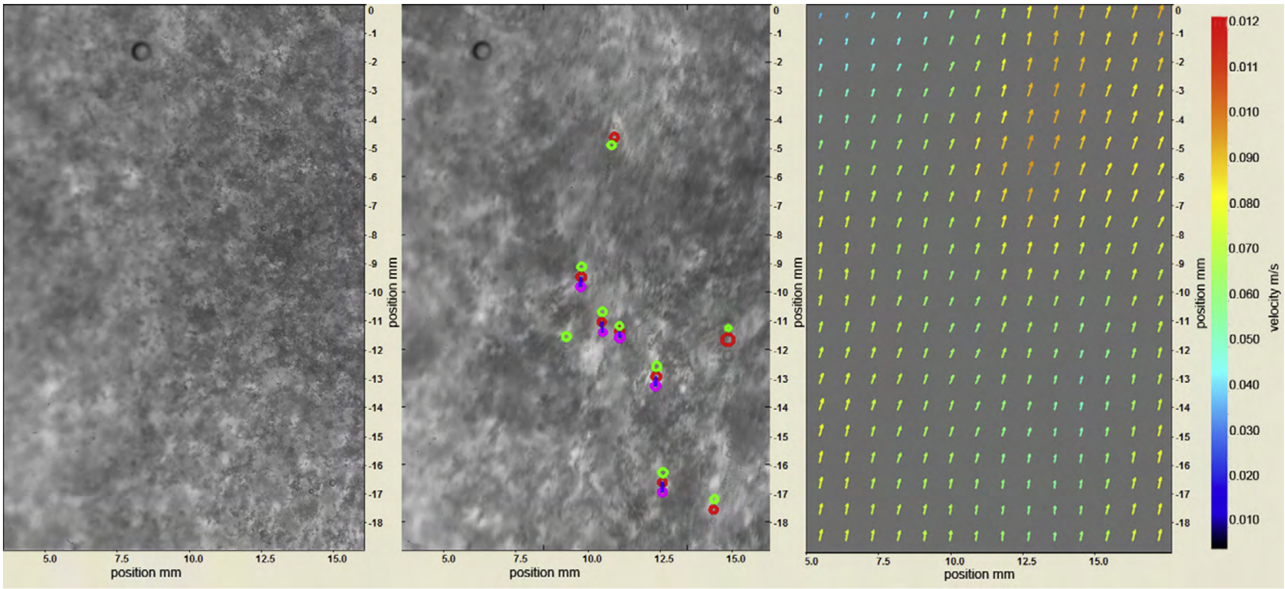

Fig. 2. Original snapshot image of microbubbles in white water (left), a multi-frame image including the detected microbubbles (middle) and the measured multiphase velocity vector field (right).

parent polycarbonate piping. Mill waters were tested at 40 °C to obtain similar physical suspension characteristics that occur in a real process environment, while tests with tap water and model suspensions took place at 20 °C.

2.3. *Measurement technique*

A high-speed digital imaging setup was used to visualise the rise of microbubbles approximately 5 mm from the bubble column wall. Imaging was limited only to near wall regions, as dispersed solid particles blocked the view deeper within the suspension. The flow was illuminated with a submerged light diffuser connected to a pulsed diode laser (Cavilux Smart, 400 W, 690 nm) with an optical fibre. Cavilux control unit synchronised the laser and the high-speed CMOS camera (PCO 1200hs) while measurements were user controlled with a laptop computer.

As shown in Fig. 1, a camera was placed outside the column opposite to the submerged light diffuser to provide shadow images of microbubbles in the flow between the light diffuser and the column wall. To eliminate image distortions due to the curved column wall, an external cubical basin filled with water was placed around the bubble column. Image scaling with a measuring rod provided a scale of 18.6 μm per image pixel. Fig. 2 shows an experimental image of microbubbles in a white-water suspension. The multi-frame image in the middle in Fig. 2 shows that the whole suspension is in motion. A multiphase velocity vector field (on the right in Fig. 2) and the size and velocity of microbubbles were computed from these image sequences.

High-speed image sequences were analysed automatically with image analysis algorithms. A velocity vector field was provided by a Fast Fourier Transform (FFT) using a cross-correlation of two consecutive images using 32 × 32 pixel interrogation areas. The cross-correlation was realised using DaVis 7.2 software. Due to the low concentration of microbubbles we can assume that the computed velocity field represents the velocity of suspended particles and fibres. The mean instantaneous velocity of the field of view is utilised as the reference velocity in the computation of the bubbles relative velocities.

Visual detection of microbubbles in the images was difficult even for a human eye. Microbubble recognition (human and automated) relies on the following assumptions: microbubbles produce dark, circular shadow images, each containing a bright spot at its centre with a sharp outline, whose curvature is nearly constant. We also assumed a size range from 50 μm to 1 mm for microbubbles and that they are rising upwards. This eliminates bubbles which are stuck on the surface of the back-light or transparent column wall, which can be seen in the left and middle images in Fig. 2.

2.4. *Bubble image recognition and tracking algorithm*

Automatic microbubble recognition algorithm included several phases that are briefly described in the following 5 step list:

1. *Image equalisation*: Image background was computed for each image with a low-frequency filter. Spatial image equalisation was obtained by dividing the image with the computed background image.
2. *Detection of microbubble outlines*: Local (5 × 5) standard deviation and a local kurtosis (4th moment) of greyscales emphasised the image areas of high greyscale variance, as local kurtosis on microbubble outline was vastly lower than that on top of a curly fibre. Due to the presence of a smooth continuous change in the curvature of a bubble circumference, the subtraction of a scaled local kurtosis image from the local standard deviation image returned an image that emphasises only the outlines of microbubbles. Finally, a search for modified local maxima was carried out to recognise the outlines of sharp microbubble images. Focus discrimination was based on the hysteresis thresholding (which is similar to the Canny edge detector) of the local maxima to locate only the in-focus bubbles.
3. *Fitting circles on microbubble outlines*: A microbubble was recognised by fitting a circle on its recognised outline. A fast and robust 3-point circle fit (a modification of Kamgar-Parsi and Netanyahu [11]) was utilised.
4. *Validation of circle fit*: Fitted circles were validated based on size range, ratio of circle perimeter to recognised outline length, a ratio of circle area to an area that overlaps with other circles and on the criteria that the centre of the circle has to have a higher original greyscale value than the inner side of the circle perimeter.
5. *Lagrangian tracking of microbubbles in image sequence*: After the recognition of microbubbles, three consecutive image frames

were analysed to link the images that belonged to the same bubble. Thus each analysed microbubble had to be detected in at least three consecutive images. Only the rising microbubbles were of interest and thus the allowed velocity range was limited upwards. A constant rise velocity and size for each bubble was assumed allowing a maximum of 20% variation in the pseudo-distance, which is defined as:

$$s_{k,j} = \sqrt{(x_{i,e}(k) - x_i(j))^2 + (y_{i,e}(k) - y_i(j))^2 + (d_{i-1}(k) - d_i(j))^2}. \quad (1)$$

The bubble coordinates and size were predicted from the previous two frames, and the predictions ($x_{i,e}$, $y_{i,e}$ and d_{i-1}) were compared to potential pair image values (x_i, y_i and d_i). The tracking method corresponds to the best-estimate method presented by Ouellette et al. [12].

2.5. Bubble size and velocity discretisation

Digital imaging technique provides plenty of information on objects that are under investigation: object size, shape and concentration in the image. The relation of an object image size and real object size is straight-forward when the objects are spherical and the geometrical calibration between the image plane and the object plane is provided, as in the case of this study. Here, the bubble size distributions were discretised into bubble size classes with equal width of 0.05 mm and size range from 0.1 to 1 mm. Larger individual bubbles that were detected were thus disregarded from further analysis.

2.6. Computation of the bubble drag coefficient

Bubble size, shape, rise velocity and the velocity of the surrounding fluid were measured with the imaging technique. Assuming a steady flow where only the drag and buoyancy forces affect the bubble motion, an estimation of the bubble drag coefficient was made. Suspensions were so dilute that the interactions of microbubbles could be neglected, but interactions between suspension dispersed particles and microbubbles clearly took place. These interactions were contained in the bubble drag coefficient. Thus, we obtained a simplified momentum equation that covers microbubble motion:

$$\sum \vec{F} = \frac{1}{2} C_D \cdot \rho_L \cdot \left| \vec{U_B} - \vec{U_L} \right| \cdot (\vec{U_B} - \vec{U_L}) \cdot A_B + (\rho_B - \rho_L) \cdot V_B \cdot \vec{g} = 0, \quad (2)$$

where A_B, V_B and U_B are the bubbles surface area, volume and rise velocity, ρ is the fluid density and U_L is the fluid velocity, obtained as the instantaneous mean fluid velocity in the measurement plane. The drag coefficient of a bubble C_D was obtained with Eq. (2) as follows:

$$C_D = \frac{-(\rho_B - \rho_L)}{\rho_L} \cdot \frac{4}{3} \cdot \frac{d_B g}{(\vec{U_B} - \vec{U_L})^2} \approx \frac{4}{3} \cdot \frac{d_B g}{(\vec{U_B} - \vec{U_L})^2}. \quad (3)$$

3. Bubble dynamics in multiphase flows

3.1. Bubble drag coefficient in pure liquids

Motion of bubbles in low Re liquids is governed by viscosity, surface tension and inertia effects. If bubbles lose their spherical shape and their motion begins to oscillate, the surface tension becomes a dominant factor. If the shape of the bubbles does not vary, as in the case of microbubbles, the larger bubble in same medium will rise faster, unless their motion becomes hindered by collision and attachment of solid particles dispersed to the flow [13,14]. The drag coefficient of a rising, spherical gas bubble with an immobile interface in a stagnant pure liquid can be predicted as a function of the bubble Reynolds number Re_B with the following correlations. Hadamard [15] and Rybczszynski [16] in Eq. (4), and Moore [17] in Eq. (5):

$$C_D = \frac{16}{Re_B}, \quad \text{for } Re_B \le 11, \quad (4)$$

$$C_D = \frac{48}{Re_B} \cdot \left(1 - \frac{2.21}{\sqrt{Re_B}}\right), \quad \text{for } 11 < Re_B \le 500, \quad (5)$$

where

$$Re_B = \frac{d_B \left| \vec{u}_B - \vec{u}_L \right|}{\nu_L}. \quad (6)$$

Mei et al. [18] devised an empirical correlation for the clean bubble drag (Eq. (7)) that matches both correlations (4) and (5) thus being valid for the entire range of Re_B presented in this study:

$$C_D = \frac{16}{Re_B} \left\{ 1 + \left[\frac{8}{Re_B} + \frac{1}{2} (1 + 3.315 Re_B^{-1/2})^{-1} \right] \right\}. \quad (7)$$

3.2. Wall effect

As the measurement took place in a confined volume vessel and relatively close to the column wall, the effect that the wall has on bubble drag needs to be quantified. As mentioned, the focal plane used was located at about 5 mm depth from the wall. The ratio of bubble diameter (d_b) and measurement position distance from column wall (d_c) for the measured microbubbles from 0.1 to 0.6 mm yields values from 0.02 to 0.12. Thus, according to Krishna et al. [19], the wall effect on bubble motion is minor. Bubble rise velocity u_B in the finite column relative to its velocity in an infinite volume, u_∞, was defined by Clift et al. [20] as:

$$\frac{u_B}{u_\infty} = 1 - \frac{9}{16} \frac{d_B}{2 \cdot l_{\text{wall}}}, \quad (8)$$

where l_{wall} is the distance of a bubble from a vertical column wall. Based on Eq. (8), the wall effect in our measurement setup increases bubble drag about 5% at 5 mm distance and 25% at 1 mm distance of the wall. Furthermore, the few investigators who have studied the wall effects have concluded [21] that the wall effect is markedly less severe on non-Newtonian power-law fluids than in Newtonian fluids under otherwise identical flow conditions.

3.3. Effect of surfactants

The negative effect of surfactants on the bubble rise velocity in a multiphase environment with the existence of impurities on a bubble surface was presented by Clift et al. [20]. This can be explained by the variation in the surface tension which forms along the bubble surface, i.e. the Marangoni effect. This causes a tangential shear stress to form on the bubble's surface resulting in a decrease of the rise velocity of the bubble. This phenomenological explanation was first described by Frumkin and Levich [22] and since reviewed by Cuenot et al. [23]. Similar results have been recently reported by Dijkhuizen et al. [24], whose observations found the drag coefficient for contaminated bubbles to be up to seven times greater than values obtained for clean bubbles. On the other hand, Okazaki [2] showed that surface active substances induce bubble surface stabilisation preventing bubble coalescence and lowers the bubble surface tension.

In many practical considerations, the bubble's surface is sufficiently contaminated and almost no-slip surface is attained. Thus we can assume that contaminated bubbles at low Reynolds number, such as in our case, rise at rates appropriate for rigid spheres and when no bubble surface motion takes place. For rigid spheres,

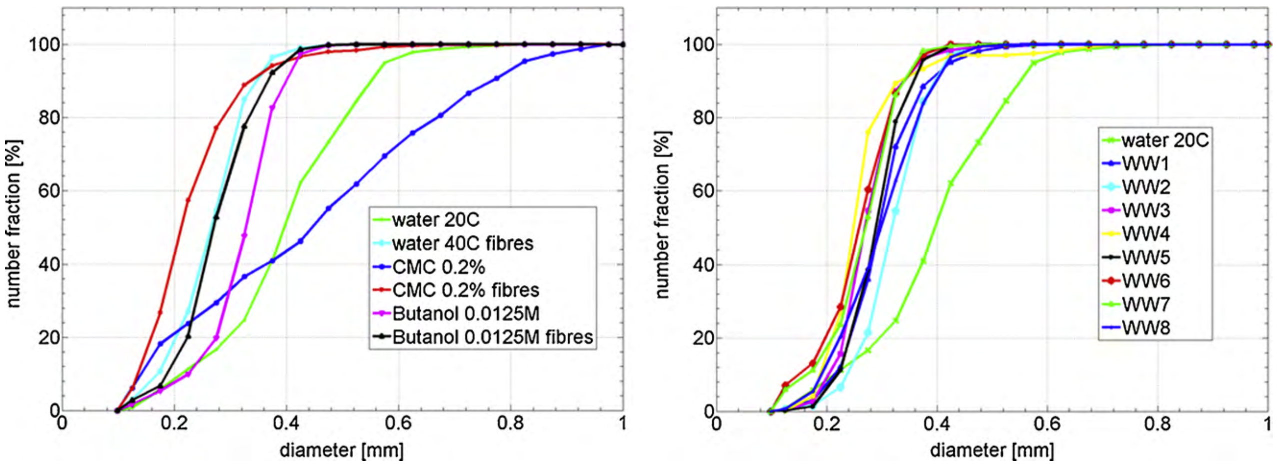

Fig. 3. Microbubble size distribution over a pressure drop for model suspensions and white waters.

the standard drag curve is estimated by the correlation by Putnam [25]:

$$C_D = \frac{24}{Re_B}\left(1 + \frac{1}{6}Re_B^{2/3}\right), \quad \text{for } Re_B < 1000. \tag{9}$$

3.4. Papermaking process waters

Bubble dynamics in multiphase suspensions (e.g. bubbly fibre suspensions) differ remarkably from the dynamics of pure air/water suspension. The phenomena in three-phase flow systems are controlled by a number of factors that are difficult to quantify and model, for example surface chemistry in gas–solid interfaces, as stated by Schulze [26]. This means that observations have typically been simplified by applying model suspensions that display similar rheological behaviour. Recently, Gomez et al. [27] presented Carbopol polymer suspension as a model fluid for pulp fibre suspensions present in papermaking processes. In non-Newtonian fluids such as Carbopol, the time dependent shear rate variation of the liquid phase may cause momentarily decrease in fluid viscosity and enable a temporally increased bubble motion.

Fibre presence in non-Newtonian multiphase flows makes the fluid greatly differ from flows involving only smooth spherical particles [14]. Fibres dampen flow velocity fluctuations and resist the flow from becoming turbulent [3,6,9]. High-speed image sequences reveal that dispersed particles and fibres often attach to microbubbles and decrease their rise velocity. Commonly, the buoyancy of a microbubble is not sufficient enough to detach bubbles from flocculated fines and fibres, and thus some bubbles tend to remain trapped within the suspension. Model fluids cannot explain the effects of the wide range of solid particles or dissolved components originating from wood or mineral fillers and fibres in the papermaking process waters [3,4,28–30]. Hence, to study the gas separation in such mediums this investigation utilises actual process suspensions.

Differences in the bubble motion between pulp suspensions were examined in the 1950s by Brecht and Kirchner [31] who found that the air holdup of groundwood stock was markedly higher than that of other stocks. This was considered dependent on the water properties of the suspension and, as noted by Stoor [1], it is probable that the hydrophobicity of the lignin-covered groundwood fibres and fines was the main contributor to these observations. Similarly in this study, the presence of mechanical pulp fines, dispersed colloidal and soluble materials in white waters 1–3 and 5 indicates that wood based extractives, organic acids and a wide array of other contaminants significantly influence the bubble motion and gas holdup [28]. A reduced rise velocity can make gas separation in these suspensions ineffective without the use of any special process stages that would add complexity into the papermaking processes [3,32,33].

4. Results and discussion

4.1. Microbubble size distributions

Microbubble size distributions were measured during a 30 s period after depressurising air-saturated suspension from 300 kPa to normal atmospheric pressure. The results of all suspensions are presented in Fig. 3. The left graph highlights the trends in microbubble size distributions for model suspensions with and without fibres. This graph indicates that the presence of fibres remarkably decreases the size of bubbles in all model suspensions. Fibre content appears to have an even higher impact on bubble size than any changes in the surface tension (n-butanol) and viscosity (CMC) of suspensions.

Microbubbles form together in swarms more strongly in fibre suspensions than in pure gas–liquid suspensions. The first bubble of a swarm rises slower than the bubbles in its wake, increasing the chances of bubble coalescence. Although increased fibre consistency is noted to promote large bubble formation as suggested by Reese et al. [3] and Heindel [6], a similar trend is not visible here. Fewer microbubbles are actually generated in suspensions containing fibres and fibre fractions than in pure liquids. The low tendency of microbubble coalescence observed by Lindsay et al. [34] and Heindel [6] was also visually observed in this study.

Takagi et al. [35,36] and Okazaki [2] report that surfactants greatly prevent microbubble coalescence. Based on this statement, we also expected to observe this in our studies with white-water suspensions. The right graph in Fig. 3 presents the bubble size distributions in tap water and white water suspensions. Bubbles in white waters are clearly smaller than those seen in tap water while the differences in the bubble size distributions between different white waters are small, despite the differences in their composition and properties. This result is in good agreement also with Tang and Heindel [28] stating that the surface-active agents present in pulp suspensions usually cause a decrease in liquid surface tension and produce smaller, more stabile bubbles. All white waters have sufficient solid contents to act as nucleation sites in the event of depressurisation and bubble formation, thus increasing the probability of small bubble formation. The oxygen saturation levels on white water aeration were all within 17–20 ppm. However, the generated microbubble concentrations were significantly lower in white waters than in model fluids as can be seen in Figs. 4 and 6.

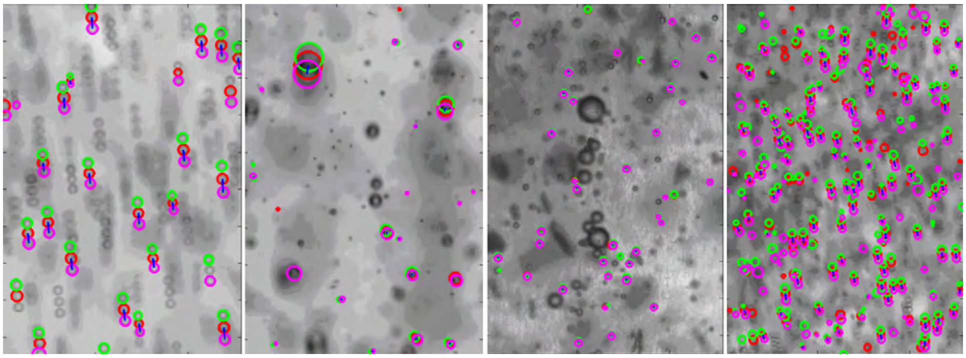

Fig. 4. Analysis images of bubbles in a selection of model water cases: from left, microbubbles in water, 0.2% CMC solution, a solution of 0.2% CMC and 0.15% fibres, and on the right, bubbles in 0.0125 M n-butanol.

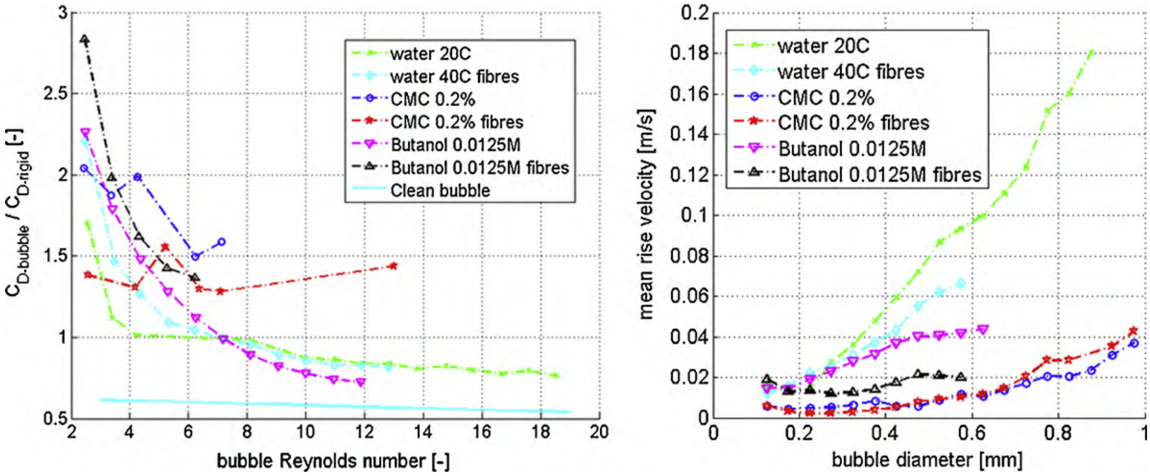

Fig. 5. Bubble drag coefficients relative to the rigid sphere (9) (left) and mean bubble rise velocities (right) according to microbubble Reynolds number and size for model suspensions.

White waters produced microbubbles with a size distribution similar to that of 0.0125 M n-butanol solution, whose surface tension and viscosity are indeed close to the values of white waters, shown in Table 1.

4.2. Bubble behaviour in model suspensions

Fig. 4 presents sequences of three consecutive images overlaid on top of each other. The circles on top of the images highlight the detected in-focus bubbles while the arrows between these bubbles correspond to their velocities. Good visibility and bubble detection was obtained in all model water cases while large quantities of out-of-focus bubbles were also seen. These and stagnant bubbles e.g. attached to the column wall, remained undetected and were not analysed. Fig. 4 demonstrates how the experimental images reveal clear differences between the suspensions. CMC solution produced large bubbles while the butanol solution induced the formation of smaller bubbles in larger quantities.

Fig. 5 presents the measured drag coefficients (C_D) with respect to the bubble Reynolds number (Re_B) according to Eq. (3), and the measured rise velocities with respect to the bubble diameter. The drag curves for a rigid sphere (Eq. (8)) and a clean bubble (Eq. (7))

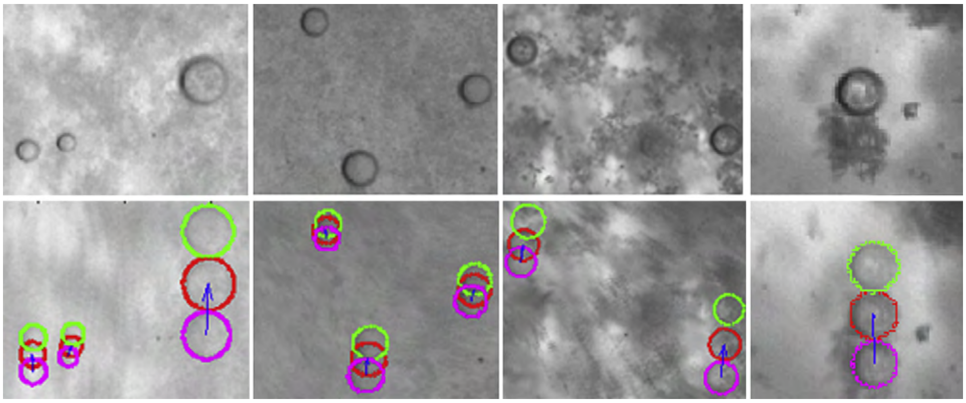

Fig. 6. Analysis images of bubbles in a selection of process water cases. Upper row shows a single image frame and the row below shows the three consecutive images where the same bubbles are identified and followed in the suspensions. Images from left: WW1, WW3, WW4 and WW6.

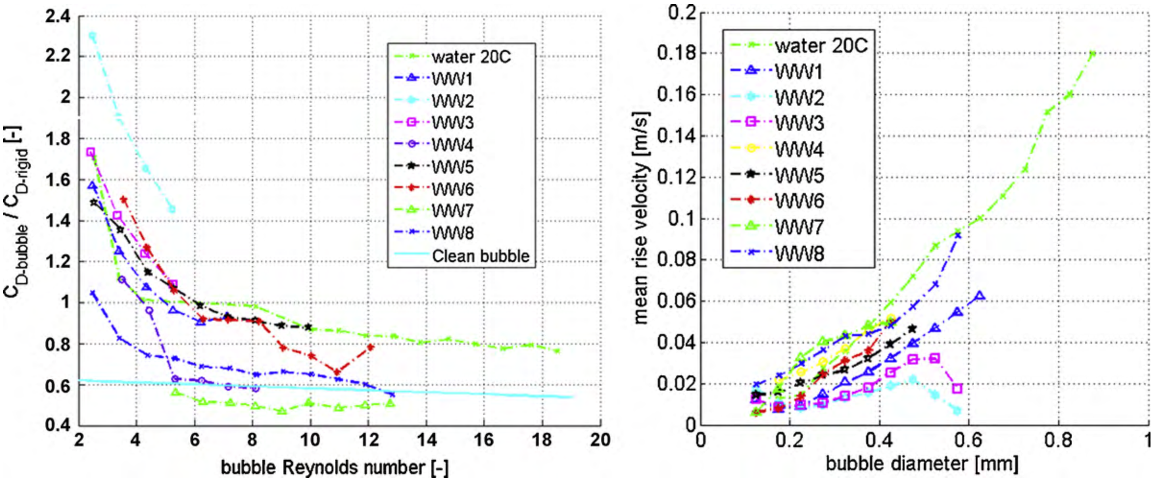

Fig. 7. Bubble drag coefficients relative to rigid sphere (9) and mean bubble rise velocities for white waters.

are shown for comparison. Results show that the bubble motion in model suspensions was governed by the drag curve of a rigid sphere rather than that of a clean bubble while bubbles rose slower in model suspensions than in tap water. As expected, the addition of kraft wood fibres further decreased the bubble rise velocities, however the studied model suspensions were so diluted that fibres had only a small effect on the bubble motion and drag. This result is in good agreement with a previous investigation [3]. It is possible that this is due to the channelling of rising bubbles to areas with the lowest consistencies and the absence of fibre entanglement and web formation, as observed in [14,28]. The results in Fig. 5 show that the viscosity of the suspension has a larger effect on microbubble rise than the presence of fibres. Bubbles in viscous (over 5.5 mPa s) CMC-solutions had by far the slowest rise velocities and the largest bubble drag coefficients.

The measured drag of microbubbles with $Re_B < 7$ was remarkably higher than the drag of a rigid sphere. This discrepancy can be explained with the presence of the surface active components that may readily adhere onto the bubble surface. The result is in good agreement with those presented by e.g. Liger-Belair et al. [37]. Their analysis for microbubble drag on supersaturated champagne and beer showed that elevated concentrations of surface active contamination (beer) in relation to bubbles with somewhat mobile surface (champagne) resulted in a significant increase in microbubble drag. They measured clearly higher drag values for microbubbles with $Re_B < 7$ than that for a rigid sphere.

4.3. Bubble behaviour in process waters

Experimental images of process waters in Fig. 6 reveal the turbid nature of these suspensions even at low solid consistencies. Original images are shown on top and the analysis results on the bottom, superimposed on three image frames. In comparison to Fig. 4, fewer bubble shadow images are seen outside the focus plane. The rightmost image shows a bubble that is dragging a fibre floc attached to its tail.

Fig. 7 presents the measured drag coefficients (C_D) and rise velocities of microbubbles in papermaking process suspensions similar to model suspensions seen in Fig. 5. The largest drag coefficients and lowest rise velocities were measured for white waters 1–3 while 5 had the highest solid content, the smallest mean particle size and the highest viscosity. The major characteristic of these waters was the presence of mechanically pulped fibres and their residue that retains a majority of the wood lignin, while a chemical fibre is primarily lignin-free. Hence, white waters 1–3 and 5 contain mechanical pulp fines and dissolved and colloidal wood components that influence water properties by e.g. lowering the surface tension [28]. Bubble dynamics in these white waters approximate the model case of 0.0125 M n-butanol solution, whose properties are close to the values of white waters.

Fine paper machine waters, labelled as white waters 4, 6, 7 and 8, consist of kraft pulp from which all lignin has been removed. The properties of these suspensions approach the values for water. Bubble rise velocities in white waters 4, 6, 7 and 8 were similar to those in tap water. In fact, microbubbles which were smaller than 0.35 mm clearly rose faster in these white waters than in tap water. This trend is also visible in drag curves (for WW's 4, 6, 7 and 8) indicating a reduction in drag. One possible explanation is that fibres dampen the flow velocities providing stagnant flow conditions for microbubble rise, similar to [3,21], whereas in the case of pure gas–liquid suspensions, the fluid velocity fluctuates considerably. The lowest drag coefficients were measured for white water 7 that had high surface tension including only low amount of solids with the largest particle size of the studied suspensions. In fact, microbubbles rose slightly faster in white water 7 than in pure water. A reason for this might be related to the non-Newtonian properties of the white water.

The presence of contaminants in general elevates the apparent viscosity of the suspensions and lowers their surface tension (see Table 1), but it also increases the rate of bubble–particle collisions and consecutive attachments that contribute to a decrease in rise velocity and elevated drag, as observed here. Phenomenon is identical to the bubble–particle interactions observed in the flotation treatments of recycled pulps and effluent waters, also in water purification outside paper industry [20,30]. In the cases of white waters 2 and 3 (Fig. 7b), the largest observed bubbles were seen to collide with fibre flocs which notably affected the motion of a few bubbles. Otherwise continuously higher velocities would be seen for larger bubbles also in these suspensions.

4.4. Microbubble drag model in white waters

With the given 8 sample waters, the analysis has insufficient data to present statistically significant causal relations of water properties to bubble rise or drag as there are multiple factors affecting bubble motions that interact with each other. Therefore, the factors cannot be treated in the analysis as fixed parameters. Furthermore, the rheology of comparable low consistency water-fibre slurries has been characterized earlier [38–40] as shear thinning non-Newtonian multiphase fluids that have complexity and inter-

Table 3
Correlation coefficients used in the drag coefficient equation for grouped white waters.

Coefficient	Group 1	Group 2
a	117	59
b	−1.73	−1.58
c	1.61	0.86

connected properties that are troublesome to compare statistically. However, the uniformity of the bubble drag coefficient curves obtained for different paper mill white waters studied in this paper justifies the utilisation of generalised models in multiphase CFD simulations.

Bubble–particle interaction is shown in previous investigations to be a function of zeta potential, particle hydrophobicity, bubble size, particle size and flocculate particle structure [41,42]. The total chemical interaction between a bubble and a particle is determined by the strength and nature of hydrophobic, electrostatic and dispersive forces acting between components. The hydrophobic interactions, which have a long effective range, are always attractive, and thus they increase adhesion between a bubble and a particle. This effectively yields to the contamination and attachment of solid particles on bubble surface, which in turn cause elevated drag. Most severely this is seen to affect the drag and holdup of the smallest bubbles [22,28,37]. This effect is commonly used in flotation applications of recycled papermaking to remove inks, adhesives and wood extractives from pulps and circulation waters. Differentiating the white waters containing mechanical pulp from the rest, the enriched extractives (i.e. resin and fatty acids and triglycerides, as dissolved or colloidal particles) is a considerable source of hydrophobic contaminants [4,7,29]. It would thus be reasonable to assume that microbubble surfaces in waters containing wood extractive residue were more contaminated and less mobile than microbubbles in kraft pulp waters. This would explain the segregation of microbubble drag into two separate groups consistent with fibre type and content.

Based on the measured data for different white waters empirical power-law correlations between the drag coefficients and the bubble Reynolds numbers are generated for the two intrinsically differing groups. Group 1 consisted of white waters 1, 2, 3 and 5 containing primarily mechanical pulp fines while group 2 (white waters 4, 6, 7 and 8) primarily containing kraft pulp fines. Obtained drag coefficients are denoted as C_{D1} and C_{D2} respectively. Correlations in their general form can be given as $f(x) = a \cdot x^b + c$, where x is the bubble Reynolds number and the correlation coefficients a, b and c are given in Table 3. The obtained empirical correlations for both white water groups are presented in Eqs. (10) and (11):

$$C_{D1} = \frac{120}{Re_B^{1.7}} + 1.6. \tag{10}$$

$$C_{D2} = \frac{60}{Re_B^{1.6}} + 0.9. \tag{11}$$

Fig. 8 shows the microbubble drag coefficient curves with respect to the bubble Reynolds number for white waters groups 1 and 2. The solid lines show the drag curves of rigid sphere and clean bubble for comparison. Fig. 8 also shows the experimental data points including the standard deviation intervals in each bubble Reynolds number class. The power-law model fits well to the experimental data and the overlap within the standard deviation spread relates to the mixed usage of mechanical and kraft pulps in some paper machines. The observed standard deviation for C_D is at its greatest for the smallest Re_B values, when the relative velocities of microbubbles are at their slowest and thus are most affected by the fluctuating fluid flow. The correlations (10) and (11) for microbubble drag coefficients in white waters are only given for a limited range of Re_B between 2 and 18. The generalised correlations serve to illustrate that microbubble drag in process waters shows significant differentiation from the drag curves of the clean bubble and rigid sphere. This should be taken into account in gas separation related process design and development.

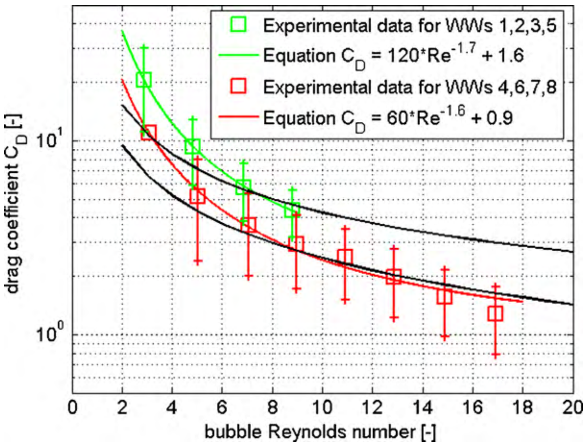

Fig. 8. Bubble drag coefficient curves for two white water groups. Measured data is presented as the mean value ± standard deviation bounds in each Re_B-class.

5. Conclusions

A novel optical high-speed imaging system was used to investigate the degree on which suspension viscosity, surface tension and solids consistency affect microbubble formation, drag and rise in model suspensions and in papermaking process suspensions in a pressurised bubble column. A robust image analysis method was developed to recognise microbubbles from the images of turbid fibre suspensions providing the first published experimental analysis on microbubble motion in paper machine filtrates.

Results showed that the presence of fibres decreases the size and formation of bubbles in a sudden pressure drop. Fibre content appears to have a greater impact on bubble size than any changes in the liquid's surface tension and viscosity. White waters of several paper mills produced microbubbles with a size distribution close to that of 0.0125 M n-butanol, whose properties are similar to the values obtained for white waters. However generalised utilisation of such model suspension to mimic paper machine white waters still requires further rheological studies.

Bubbles rose slower in model suspensions than in tap water. The addition of wood fibres further decreased the bubble rise velocities. Bubbles in viscous (over 5.5 mPa s) CMC-solutions had by far the slowest rise velocities. These results reveal that liquid phase viscosity has a larger effect on microbubble motion than the presence of wood fibres in low consistency of 0.15%.

In paper machine white waters, the measured microbubble drag coefficients deviated significantly from the drag models of a rigid sphere and clean bubble. However, measurements in white waters were similar to 0.0125 M n-butanol emphasising the significance of viscosity and surface tension on the drag of microbubbles. Measured differences between the white waters can be explained by these, solids content and properties such as hydrophobicity of the solid particles. White waters were distinguished in groups that contain either mechanical or lignin-free kraft pulp fines and specific bubble drag coefficient curves were formulated for both groups. Hindering effect of hydrophobic colloidal and solid particles, including short fibres, were seen significant especially to the drag of small microbubbles. This occurrence was contributed to bubble surface contamination by surfactants and moreover to attachment of fibre flocs on bubbles, which was also verified by visual observation. These empirical drag coefficients will prove to be particularly useful in the multiphase CFD simulations of papermaking and gas separation processes.

Acknowledgements

Authors would like to thank TEKES (The Finnish Funding Agency for Technology and Innovation), PaPSaT graduate school and the Academy of Finland for financially supporting this research. Also the kind assistance in white water analyses of Ms. Sanna Haavisto from the VTT Technical Research Centre of Finland is appreciated.

References

[1] T. Stoor, Air in pulp and papermaking processes, Dissertation, University of Oulu, 2006.

[2] S. Okazaki, The velocity of air bubble ascending in aqueous solution of surface active substance and inorganic electrolyte, Colloid Polym. Sci. 185 (1962) 154–157.

[3] J. Reese, P. Jiang, L.-S. Fan, Bubble characteristics in three-phase systems used for pulp and paper processing, Chem. Eng. Sci. 51 (2006) 2501–2510.

[4] T.M. Garver, T.B. Xie, H. Kenneth, Variation of white water composition in a TMP and DIP newsprint paper machine, Tappi J. 80 (1997) 163–173.

[5] A. Margaritis, D.W. te Bokkel, D.G. Karamanev, Bubble rise velocities and drag coefficients in non-Newtonian polysaccharide solutions, Biotechnol. Bioeng. 64 (1999) 257–266.

[6] T.J. Heindel, Bubble size in concurrent fiber slurry, Ind. Eng. Chem. Res. 41 (2002) 632–641.

[7] M.A. Hubbe, Water and papermaking. 2: White water components, Paper Technol. 48 (2007) 31–40.

[8] M. Honkanen, P. Saarenrinne, T. Stoor, J. Niinimäki, Recognition of highly overlapping ellipse-like bubble images, Meas. Sci. Technol. 16 (2005) 1760–1770.

[9] M. Honkanen, K. Marjanen, Analysis of the overlapping images of irregularly-shaped particles, bubbles and droplets, in: Proc. of Int. Conf. on Multiphase Flow, Paper 559, Leipzig, Germany, 2007.

[10] M. Honkanen, H. Eloranta, P. Saarenrinne, Digital imaging measurement of dense multiphase flows in industrial processes, Flow Meas. Instrum. 21 (2010) 25–32.

[11] B. Kamgar-Parsi, N.S. Netanyahu, A nonparametric method for fitting a straight line to a noisy image, IEEE Trans. Pattern Anal. Mach. Intell. 11 (1998) 998–1001.

[12] N.T. Ouellette, H. Xu, E. Bodenschatz, A quantitative study of three-dimensional Lagrangian particle tracking algorithms, Exp. Fluids 40 (2006) 301–313.

[13] N.M.S. Hassan, M.M.K. Khan, M.G. Rasul, A study of bubble trajectory and drag co-efficient in water and non-Newtonian fluids, WSEAS Trans. Fluid Mech. 3 (2008) 261–270.

[14] H. Cui, J.R. Grace, Flow of fibre suspension and slurries: a review, Int. J. Multiphase Flow 33 (2007) 921–934.

[15] J. Hadamard, Mouvement permanent lent d'une sphère liquide et visqueuse dans un liquide visqueux, C.R. Math. Seances Acad. Sci. 152 (1911) 1735–1738.

[16] W. Rybcszynski, Über die fortschreitende Bewegung einer flüssigen Kugel in einem zähen Medium, Bull. Acad. Sci. Cracovie. A 40 (1911).

[17] D.W. Moore, The boundary layer on a spherical gas bubble, J. Fluid Mech. 16 (1963) 161–176.

[18] R. Mei, J.F. Klaussner, C.J. Lawrence, A note on the history force on a spherical bubble at finite Reynolds number, Phys. Fluids 6 (1994) 418–420.

[19] R. Krishna, M.I. Urseanu, J.M.V. Baten, J. Ellenberger, Wall effects on the rise of single gas bubbles in liquids, Int. Commun. Heat Mass Transfer 26 (1999) 781–790.

[20] R. Clift, J.R. Grace, W.E. Weber, Bubbles, Drops, and Particles, Academic Press, New York, 1978.

[21] R.P. Chhabra, Bubbles, Drops, and Particles in non-Newtonian Fluids, CRC Press, Boca Raton, 2006.

[22] A. Frumkin, V.G. Levich, On surfactants and interfacial motion, Zh. Fiz. Khim. 21 (1947) 1183–1204.

[23] B. Cuenot, J. Magnaudet, B. Spennato, The effects of slightly soluble surfactants on the flow around a spherical bubble, J. Fluid Mech. 339 (1997) 25–53.

[24] W. Dijkhuizen, I. Roghair, M. Van Sint Annaland, J.A.M. Kuipers, DNS of gas bubbles behaviour using an improved 3D front tracking model-Drag force on isolated bubbles and comparison with experiments, Chem. Eng. Sci. 65 (2010) 1415–1426.

[25] A. Putnam, Integrable form of droplet drag coefficient, ARS J. 31 (1961) 1467.

[26] H.J. Schulze, Physico-Chemical Elementary Processes in Flotation, Elsevier, Amsterdam, 1983.

[27] C. Gomez, B. Derakhshandeh, S.G. Hatzikiriakos, C.P.J. Bennington, Carbopol as a model fluid for studying mixing of pulp fibre suspensions, Chem. Eng. Sci. 65 (2010) 1288–1295.

[28] C. Tang, T.J. Heindel, Effect of fiber type on gas holdup in a concurrent air–water–fiber bubble column, Chem. Eng. J. 111 (2005) 21–30.

[29] P. Valto, J. Knuutinen, R. Alén, M. Rantalankila, J. Lehmonen, A. Grönroos, J. Houni, Analysis of resin and fatty acids enriched in papermaking process waters, Bioresources 5 (2010) 172–186.

[30] A.V. Nguyen, Particle–bubble encounter probability with mobile bubble surfaces, Int. J. Miner. Process. 55 (1998) 73–86.

[31] W. Brecht, U. Kirchner, Über den luftgehalt in papierstoffsuspensionen, Wochenblatt für Papierfabrikation 87 (1956) 295–305.

[32] T.M. Helle, Qualitative and quantitative effects of gas content on papermaking, Paper Timber 82 (2000) 457–463.

[33] A. Haapala, T. Stoor, H. Liimatainen, M. Nelo, J. Niinimäki, Passive white water deaeration efficiency in open channel flow, Appita J. 62 (2009) 105–109.

[34] J.D. Lindsay, S.M. Ghiaasiaan, S.I. Abdel-Khalik, Macroscopic flow structure in a bubbling paper pulp-water slurry, Ind. Eng. Chem. Res. 34 (1995) 3342–3354.

[35] S. Takagi, T. Ogasawara, Y. Matsumoto, The effects of surfactant on the multiscale structure of bubbly flows, Philos. Trans. R. Soc. A 366 (2008) 2117–2129.

[36] S. Takagi, T. Ogasawara, M. Fukuta, Y. Matsumoto, Surfactant effect on the bubble motions and bubbly flow structures in a vertical channel, Fluid Dyn. Res. 41 (2009) 065003.

[37] G. Liger-Belair, R. Marchal, B. Robillard, T. Dambrouck, A. Maujean, M. Vignes-Adler, P. Jeandet, On the velocity of expanding spherical gas bubbles rising in line in supersaturated hydroalcoholic solutions: application to bubble trains in carbonated beverages, Langmuir 16 (2000) 1889–1895.

[38] J-P.T. Huhtanen, R.J. Karvinen, Interaction of non-Newtonian fluid dynamics and turbulence on the behavior of pulp suspension flows, Ann. Trans. Nord. Rheol. Soc. 13 (2005) 177–186.

[39] C.J.S. Petrie, The rheology of fibre suspensions, J. Non-Newtonian Mech. 87 (1999) 369–402.

[40] E. Lasseuguette, D. Roux, Y. Nishiyama, Rheological properties of microfibrillar suspension of TEMPO-oxidized pulp, Cellulose 15 (2008) 425–433.

[41] M. Han, W. Kim, S. Dockko, Collision efficiency factor of bubble and particle DAF: theory and experimental verification, Water Sci. Technol. 43 (2001) 139–144.

[42] B. Johansson, G. Strom, Surface chemistry of flotation deinking: effect of various chemical conditions on ink agglomerate character and flotability, Nord. Pulp. Pap. J. 13 (1998) 37–49.